Article

Improving Mechanical Properties of Mg-Al-RE Alloys with the Formed Dimples of $Al_{10}Mn_2RE$ Particles and Activated Pyramidal <*a*> Slip with Mn Additions

Jiandong Yang [1,2], Wuxiao Wang [1,*], Min Zhang [1,*], Jian Liu [3] and Shaoyong Qin [1]

[1]   School of Material Science and Engineering, Xi'an University of Technology, Xi'an 710048, China; yangjiandong7c@163.com (J.Y.); qinshaoyong@xaut.edu.cn (S.Q.)
[2]   Xi'an Aeronautical Polytechnic Institute, Xi'an 710089, China
[3]   Faculty of Printing, Packaging and Digital Media, Xi'an University of Technology, Xi'an 710054, China; liujian@xaut.edu.cn
[*]   Correspondence: wangwx@xaut.edu.cn (W.W.); zhmmn@xaut.edu.cn (M.Z.)

Abstract: The effects of Mn addition on the room temperature tensile strength and deformation mechanisms of as-cast Mg-8Al-1Nd-1.5Gd-xMn alloys (x = 0, 0.3, 0.5, 1.0 wt.%) are investigated in this paper. The results indicate that the addition of Mn contributes to the precipitation of Al-Mn-RE intermetallics and the refinement of α-Mg matrices, thereby improving the tensile strength of the 1.0 Mn alloy at 190 MPa. The fracture mechanism of Mn-containing alloys transforms from a cleavage fracture to a ductile fracture as the Mn content increases from 0.3 to 1.0 wt.%. The presence of intermetallic particles in the dimples confirms the hindrance effect of $Al_{10}Mn_2$ (Nd,Gd) on dislocation slips. The novel technology of in-grain misorientation axes (IGMAs) is used to identify activated slip modes and deformation twins. It can be concluded that the activated pyramidal <*a*> slip during tensile deformation significantly promotes the ductility of the 1.0 Mn alloy with an elongation rate of 9.8%. It is worth noting that reducing the coarse $\{10\bar{1}2\}$ tensile twins and enhancing the proportion of $\{10\bar{1}1\}$ compressive twins and $\{10\bar{1}1\}$-$\{10\bar{1}2\}$ double twins contributes to maintaining the continuous plastic deformation of Mg alloy.

Keywords: magnesium alloy; mechanical properties; fracture mechanism; dislocation slip; deformation twin

1. Introduction

Mg-Al alloys have been extensively applied in the aerospace and automobile industries given their low density, excellent castability, and mechanical processing properties [1–3]. However, their mechanical properties and creep resistance deteriorate rapidly as their service temperature exceeds 120 °C because of softened and coarsened β-$Mg_{17}Al_{12}$ at high temperatures [4]. Mg-Al-RE-based alloys are applied to powertrain components in automobiles because of their excellent high-temperature creep resistance. This is mainly attributed to Al_2RE and $Al_{11}RE_3$ intermetallics, the dominant strengthening phases, which are mainly distributed at grain boundaries and can effectively impede dislocation motion and grain boundary sliding [5–8]. The addition of rare earth (RE) elements can significantly enhance the tensile strength and creep resistance of these alloys while also sacrificing elongation [9]. To achieve a balance between tensile strength and elongation, manganese (Mn) is widely used as a trace element additive in Mg-Al-RE alloys. Using grain refinement on as-cast Mn-containing magnesium alloys is an important way to improve their deforming behavior [10,11]. Simultaneously, the addition of Mn can promote the precipitation of Al-Mn-RE intermetallics, which mainly form Al_8Mn_5, $Al_{10}RE_2Mn_7$, and $Al_{12}RE_2Mn_5$ in Mg-Al-RE-Mn alloys [9,12–14]. Mn is prone to reacting with Al, Nd, and Gd elements and can form binary or ternary phases, thereby continuously consuming the concentration of

Al and reducing the β-Mg$_{17}$Al$_{12}$ phase content. Mn-induced grain refinement and diverse intermetallic compounds enable Mg-Al-RE-Mn alloys to exhibit excellent comprehensive mechanical properties [15–17]. It is generally believed that the addition of Mn can improve the tensile strength and elongation of magnesium alloys, mainly because of fine-grain strengthening. In addition, adding a solid solution of Mn atoms to a magnesium matrix leads to a decrease in the c/a ratio, which helps to initiate prismatic <*a*> slip and thus improves the plastic deformation ability of Mg alloys. Mg alloys are mainly subject to basal <*a*> slip at ambient temperatures, causing poor plasticity. Consequently, the deformation twins are activated to coordinate the deformation of the *c*-axis and improve the plastic deformation ability.

Currently, the dominant method for distinguishing dislocation structures is based on the invisibility criterion, $g \cdot b = 0$ [18]. In terms of the micro-mechanisms of tensile fractures, previous studies have indicated that transgranular fractures and intergranular fractures are the main failure modes of Mg-Al-based alloys [19]. Transgranular fractures are susceptible to propagating at $\{10\bar{1}1\}$ twin grain boundaries in failed specimens with twin planes as the main cleavage planes [20]. The promoting effect of Mn on prismatic slips is still controversial, and the effect of different deformation twins ($\{10\bar{1}2\}$ tensile twins, $\{10\bar{1}1\}$ compressive twins, and $\{10\bar{1}1\}$-$\{10\bar{1}2\}$ secondary twins) on the elongation of the alloys has not been accurately determined [21,22]. At present, the analysis of tensile fracture mechanisms is mainly based on the observation of the fracture surface of tensile specimens, which can be classified as cleavage fractures or ductile fractures from a macro perspective. Unfortunately, the analysis of micro-deformation mechanisms, especially in the characterization of activated slip systems and deformation twins, is still lacking. The novel technology of in-grain misorientation axes (IGMAs) is proposed to analyze the dominant deformation mechanisms of basal slips, prismatic slips, and pyramidal slips in deformed grains [23–26]. Compared with the direct observation of dislocation structures using two weak-beam dark fields (WBDFs), IGMAs are more efficient in identifying slip systems by utilizing the intensity distribution of specific crystal axis rotations (1.2–2°) caused by slipping [25,27].

In this work, as-cast Mg-8Al-1Nd-1.5Gd-*x*Mn (*x* = 0, 0.3, 0.5, 1.0 wt.%) alloys are designed to investigate the influence of RE (Nd, Gd) and Mn composite modification on the tensile fracture mechanisms of Mg-Al alloys. The microstructures and fracture morphology of the tensile failure specimens are systematically characterized, and the underlying deformation mechanisms are analyzed by identifying the activated dominant slip and twins. The results are of profound significance for balance strength and plasticity in Mg-Al-RE alloys.

2. Experimental Material and Procedures

The specific alloys were prepared with magnesium ingot (99.99 wt.%), aluminum ingot (99.99 wt.%), Mg-30 Gd, Mg-30 Nd, and Mg-15 Mn (wt.%) intermediate alloys (Shanxi Yinguang Huasheng Magnesium Industry Co., Ltd., Yuncheng, China) Magnesium and aluminum ingots were initially melted in a resistance furnace at 710 °C in a protective atmosphere of Ar, and then the intermediate alloys were added for 30 min of insulation until the alloy was completely melted. The chemical composition of the alloys was homogenized through mechanical stirring. The molten Mg alloys were directly poured into a steel mold (preheated at 150 °C for 12 h) at 710 °C to obtain circular ingots with diameters of 50 mm. The alloy compositions were confirmed via inductively coupled plasma optical emission spectroscopy (ICAP6300 Radial, Thermo Fisher Scientific, MA, USA) as shown in Table 1. The prepared Mg-8Al-1Nd-1.5Gd-*x*Mn (*x* = 0, 0.3, 0.5, 1.0 wt.%) alloys are abbreviated as Mn-free, 0.3 Mn, 0.5 Mn, and 1.0 Mn alloys.

Table 1. Composition of designed alloys and corresponding values measured via ICP.

Alloys	Abbreviation	Elemental Composition (wt.%)				
		Al	Gd	Nd	Mn	Mg
Mg-8Al-1Nd-1.5Gd-0.0Mn	Mn-free	8.09	1.48	1.13	0.0	Bal.
Mg-8Al-1Nd-1.5Gd-0.3Mn	0.3 Mn	7.98	1.51	1.06	0.31	Bal.
Mg-8Al-1Nd-1.5Gd-0.5Mn	0.5 Mn	8.11	1.46	0.97	0.49	Bal.
Mg-8Al-1Nd-1.5Gd-1.0Mn	1.0 Mn	8.13	1.52	1.0	1.1	Bal.

Tensile tests were conducted on a computer-controlled material testing machine with a tensile rate of 0.5 mm/min at ambient temperature. The average value of three tensile tests was taken for each specimen, as shown in Figure 1, and the deformation displacement was measured with an extensometer (the gauge length was 10.1 mm).

$$\text{e} = \frac{L_K - L_0}{L_0} \times 100\%$$

where e is percentage elongation, L_0 is the original gauge length, and L_K is the final gauge length after rupture.
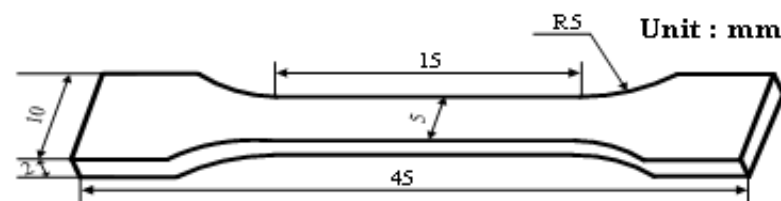
Figure 1. Schematic diagram of sample size for uniaxial tensile tests.

The microstructure was characterized via X-ray diffraction (XRD) (SmartLab, Rigaku, Tokyo, Japan) with a scanning step of 5°/min and an SEM-6700F scanning electron microscope (SEM) equipped with an electron-backscattered diffraction (EBSD) and energy-dispersive spectrometer (EDS) (JEOL, Tokyo, Japan). The EBSD samples were electropolished with 10% perchloric acid ethanol electrolyte under a voltage of 30 V (10 °C) for 15 s, and then ion-polished at a voltage of 6 kV and an angle of 2°. The samples were polished at two points near and far away from the fracture, and each point was polished for 40 min. EBSD data were processed using Channel 5(Oxford Instruments, Abbington, Oxfordshire, UK) and slip systems and twins during tensile deformation were identified using IGMA technology. For TEM, the upper and lower surfaces of the samples were alternately thinned to allow for transparency at 3 kV, and FIB sample preparation was completed.

3. Results and Discussion

3.1. Microstructure of As-Cast Mg-8Al-1Nd-1.5Gd-xMn Alloys

As shown in the typical XRD pattern of as-cast alloys in Figure 2, the studied alloys were composed of α-Mg, β-$Mg_{17}Al_{12}$, Al_2RE, and Mn-containing intermetallic compounds combined with EDS (Table 2). The EDS results of points B and E exhibited a high amount of Mg, which might originate from the Mg matrix. There were no discernible diffraction peaks from the Al_8REMn_4 and Al_{12}RE$_2Mn_5$ phases in the results, as firstly, the diffraction peaks of high-strength Mg caused the diffraction peaks of these two phases to be submerged, and secondly, the relatively low content of these two phases reduced the detection sensitivity. As shown in Figure 3a, massive, continuous island-like eutectic β-$Mg_{17}Al_{12}$ is distributed in the inter-dendritic region, and partial, completely divorced eutectic β-$Mg_{17}Al_{12}$ is scattered in the grains. In comparison with the Mn-free alloy, the volume fraction of intermetallic compounds obviously increased in the 0.3 Mn alloys (Figure 3b). Furthermore, the addition of 0.5 wt.% Mn transformed coarse eutectic β-$Mg_{17}Al_{12}$ into a granular divorced eutectic form while reducing the quantity of coarse Al_2 (Nd,Gd) and increasing needle-shaped Al_{11}

(Nd,Gd)$_3$ (Figure 3c). Compared to the 0.5 Mn alloy, the 1.0 Mn alloy achieved a significant increase in Al-Mn-RE phases and a decrease in the content of eutectic β-Mg$_{17}$Al$_{12}$, as shown in Figure 3d. This is mainly due to the preferential precipitation of Mn-containing intermetallics at the solid–liquid front, which consumes a large amount of Al atoms and reduces the concentration of Al atoms involved in the formation of β-Mg$_{17}$Al$_{12}$, thereby reducing the volume fraction of the coarsened eutectic phase [28]. Compared with the Mn-free alloy, the Al$_8$ (Nd,Gd)Mn$_4$, Al$_{12}$ (Nd,Gd)$_2$Mn$_5$, Al$_{11}$ (Nd,Gd)$_3$, and tiny β-Mg$_{17}$Al$_{12}$ phases shown in Mn-containing alloys replace the coarsened eutectic β-Mg$_{17}$Al$_{12}$ that deteriorates the mechanical properties of the alloy. Both granular Al$_{12}$ (Nd,Gd)$_2$Mn$_5$ and needle-shaped Al$_{11}$ (Nd,Gd)$_3$ are beneficial for improving the strength of the alloy [29]. The preferentially solidified Al$_2$ (Nd,Gd) and Al-Mn-RE phases are distributed at the solid–liquid front, hindering the growth of α-Mg matrix grains and ultimately refining their grains.
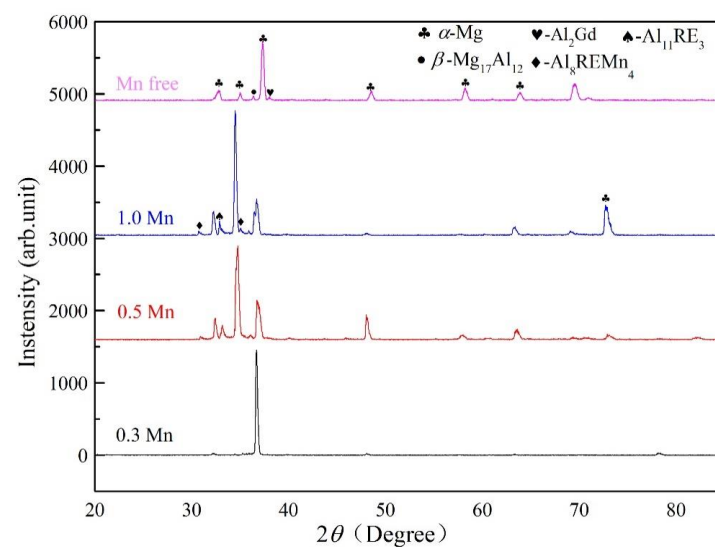

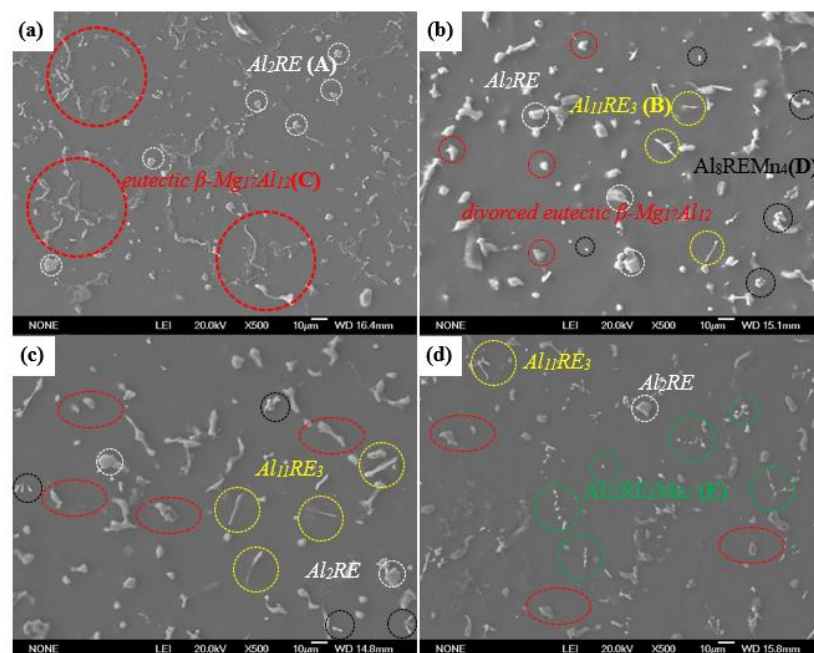**Figure 2.** X-ray diffraction patterns of as-cast Mg-8.0Al-1.0Nd-1.5Gd-xMn (wt.%) alloys.

Figure 3. Typical SEM images of Mg-8Al-1Nd-1.5Gd-xMn alloy*s*: (**a**) Mn-free, (**b**) 0.3 Mn, (**c**) 0.5 Mn, and (**d**) 1.0 Mn.

Table 2. Measured compositions of various intermetallics in the 1.0 Mn alloy.

Isomorphous Phase	Composition (at. %)				
	Mg	**Al**	**Nd**	**Gd**	**Mn**
A (Al_2RE)	13.83	61.13	9.50	14.21	1.33
B ($Al_{11}RE_3$)	57.43	32.93	4.0	5.15	0.54
C (β-$Mg_{17}Al_{12}$)	67.76	38.04	—	—	—
D (Al_8REMn_4)	9.54	55.90	2.56	5.91	26.08
E ($Al_{12}RE_2Mn_5$)	57.59	16.55	1.17	0.95	5.74

3.2. Mechanical Properties of Mg-8Al-1Nd-1.5Gd-xMn Alloys

The typical engineering stress–strain curves are illustrated in Figure 4, and the mechanical properties of Mg-8Al-1Nd-1.5Gd-xMn alloys are illustrated in Table 3. The tensile tests of the as-cast alloys indicate a continuous increment in tensile strength and elongation as the Mn content increases. It is worth noting that the yield strength of the 0.5 Mn alloy was slightly higher, while there were no significant differences among the other alloys. This indicates that the addition of Mn had little effect on the yield strength of the alloy. However, compared to the yield strength, the tensile strength of the alloy varied significantly. The tensile strength and elongation increased from 89.9 to 110.9 MPa and from 5.1% to 9.8%, respectively. It can be concluded that the addition of Mn to Mg-8Al-1Nd-1.5Gd alloys improves their tensile strength and plastic deformation ability. Compared to the Mn-free alloy, the tensile strength and elongation of the 1.0 Mn alloy were increased by 25.8% and 92.2%, respectively. Meanwhile, the mechanical properties of various high-aluminum Mg alloys prepared with gravity casting are listed in Table 4. It can be seen that the 1.0 Mn alloy studied in this work exhibited excellent comprehensive mechanical properties, especially the elongation that reflects the plastic deformation ability of the alloy.
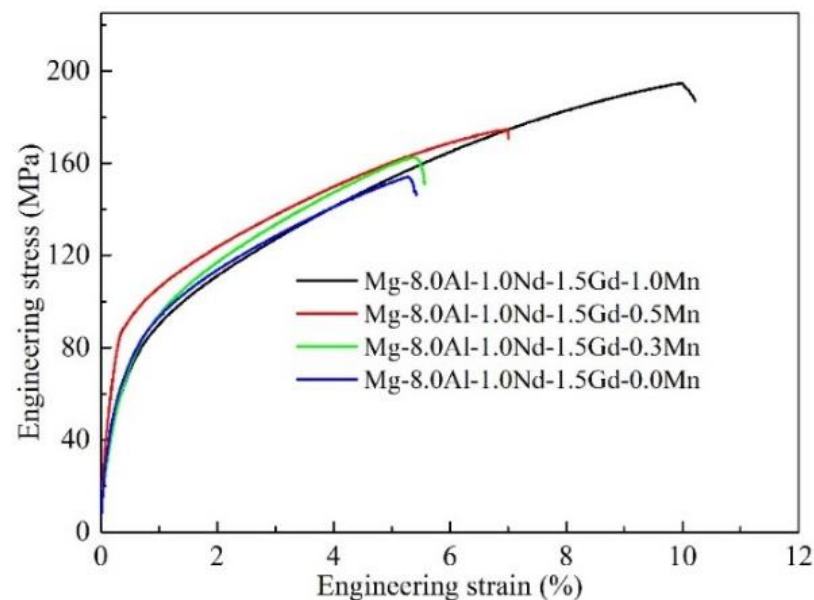

Figure 4. Tensile performance curves of the specific alloys.

Table 3. Mechanical properties of the alloys tested at room temperature.

Specimens	Tensile Strength/MPa	Elongation/%	Yield Strength/MPa
0.0 Mn	154.2^{+3}_{-1}	$5.1^{+0.3}_{-0.2}$	101.4^{+3}_{-2}
0.3 Mn	162.2^{+2}_{-1}	$5.4.2^{+0.5}_{-0.1}$	104.2^{+2}_{-1}
0.5 Mn	174.5^{+4}_{-2}	$6.9^{+.06}_{-0.2}$	110.9^{+5}_{-3}
1.0 Mn	194.6^{+5}_{-2}	$9.8^{+0.74}_{-0.3}$	100.2^{+4}_{-2}

Table 4. Tensile properties for gravity-die-cast Mg alloys.

Alloy (wt.%) Gravity Die Casting	Tensile Strength (MPa)	Yield Strength (MPa)	Elongation (%)	Ref.
AZ91	155~190	80~100	3.2~4.9	[30–32]
Mg-9Al-RE	165~187	84~116	4.0~6.4	
AZ80	160~182	95	5.1	[33–35]
AZ80-RE	182~191	90~110	5.6~7.9	
Mg-8Al-1Nd-1.5Gd-1.0Mn	199.6~192.6	104.2~98.2	9.5~10.5	

To analyze the distinct mechanical properties of the alloys with different Mn content, the quantity, types, and grain size of precipitated intermetallics were also taken into account. The EBSD diagrams in Figure 5a,b illustrate that the average grain size of the α-Mg matrix in the 0.3 Mn alloy was 200 μm, while the corresponding grain size of the 1.0 Mn alloy was 152 μm. The particle size of intermetallic compounds in the 1.0 M alloy was the smallest, and the proportions of coarse Al_2 (Nd,Gd) and Al_8REMn_4 phases were relatively low, thus exhibiting excellent mechanical properties. According to the Hall–Petch relationship ($\Delta\sigma_{ys} = kd^{-1/2}$), where σ_{ys} is the yield stress, d is the average grain size, and k is the stress concentration factor, the enhancement of tensile strength for Mn-containing alloy is closely related to grain refinement, which includes refinement of eutectic β-$Mg_{17}Al_{12}$ and α-Mg matrix grains [36]. In addition, various dispersed Al-Mn-RE ($Al_{12}RE_2Mn_5$) and Al-RE ($Al_{11}RE_3$) intermetallic compounds effectively hinder the slip of dislocations and improve the tensile strength of the alloys [14,37]. To summarize, coarse eutectic β-$Mg_{17}Al_{12}$ in Mn-free alloys is the main factor that deteriorates the mechanical properties of the alloy. By adding Mn, the coarse eutectic β-$Mg_{17}Al_{12}$ is transformed into fine, granular, divorced eutectic structures. Although blocky Al_2RE and $Al_{11}RE_3$ phases were detected in 0.3 Mn and 0.5 Mn alloys, the size and number of eutectic β-$Mg_{17}Al_{12}$ phases were significantly decreased. In addition, the precipitation of $Al_{11}RE_3$ had a positive effect on improving the tensile strength of the alloy.
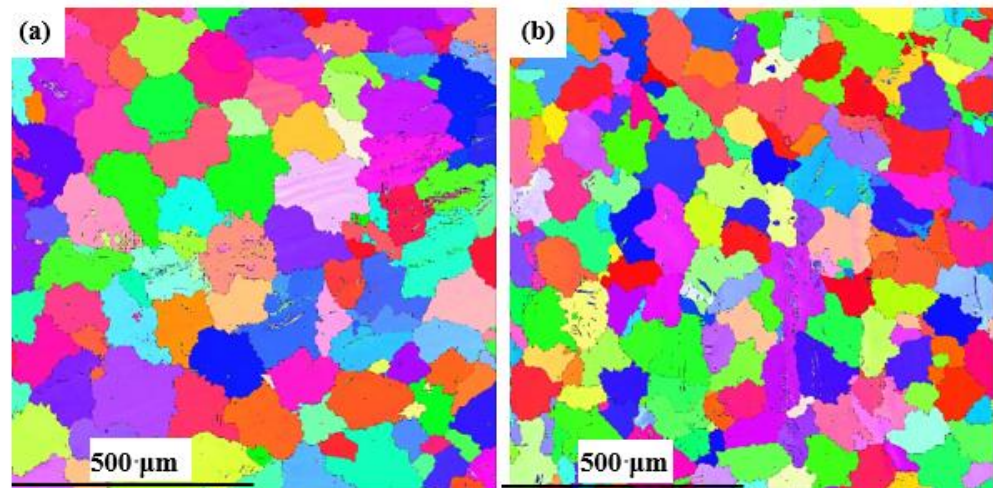
Figure 5. EBSD maps with grain boundaries of as-cast alloys: (**a**) Mg-8Al-1Nd-1.5Gd-0.3Mn; (**b**) Mg-8Al-1Nd-1.5Gd-1.0Mn.

3.3. Fracture Surface Characterization of Mg-8Al-1Nd-1.5Gd-xMn Alloys

Figure 6a–d show the metallographic images of the longitudinal tensile fracture surface of Mg-8Al-1Nd-1.5Gd-xMn (x = 0, 0.3, 0.5, 1.0 wt.%) alloys. The fracture surface of the tensile specimens exhibited a typical serrated morphology, and the fluctuation height difference of the crack propagation path in the Mn-containing specimens was 120 to 210 μm (marked by yellow parallel lines). This indicates that more energy needs to be consumed during the dynamic fracture process [38]. The fracture surface of the Mn-free alloy is rela-

tively flat, so the demand for energy during crack propagation is relatively low. Figure 6e,f show the macroscopic cracks in the tensile failure specimens initially forming and extending from the grain boundary. In addition, a small amount of trans-granular fracture mainly extended along the eutectic β-Mg$_{17}$Al$_{12}$ distribution direction, and the crack direction was perpendicular to the tensile direction. As shown in Figure 7a–d, the cavities were mainly concentrated in the fragmentation of coarse eutectic β-Mg$_{17}$Al$_{12}$ and aggregated to form microcracks [39]. Accordingly, reducing the content of eutectic β-Mg$_{17}$Al$_{12}$ and refining intermetallic compounds are effective means of improving mechanical properties. Figure 7e shows that the Al$_2$RE and Al$_{11}$RE$_3$ are sheared into several parts under stress. Due to the high elastic moduli of these two phases and their excellent bonding strength with the α-Mg matrix, voids or fragments did not form, effectively preventing crack propagation. Figure 7f shows the propagation path of transgranular cracks in α-Mg, indicating that the main crack initially propagated from β-Mg$_{17}$Al$_{12}$ and propagated along the interface with the α-Mg matrix. This indicates that the eutectic β-Mg$_{17}$Al$_{12}$ is the main source of cracks. Al$_2$RE and Al$_{11}$RE$_3$ can effectively suppress crack propagation, thereby improving the strength of the alloy.

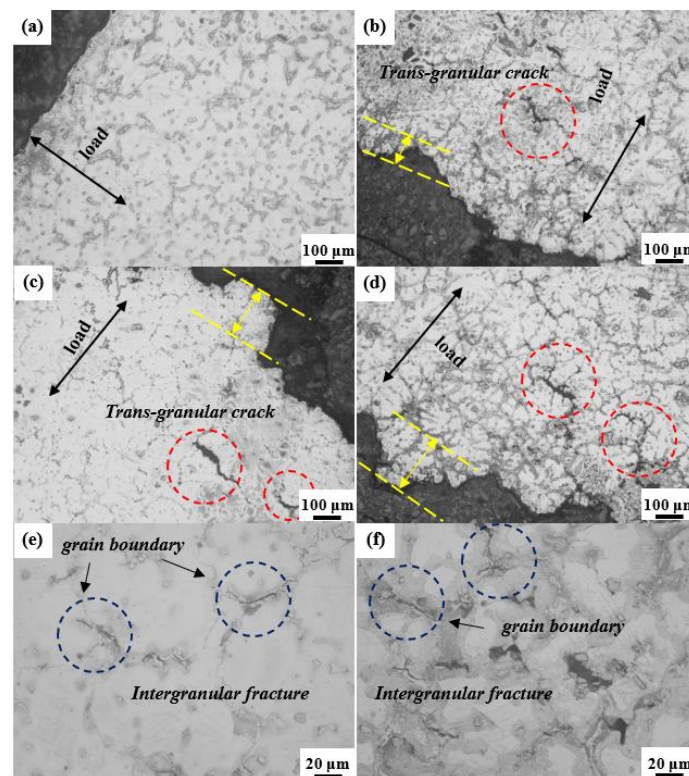**Figure 6.** Longitudinal microstructures of fracture: (**a**) Mn-free; (**b**) 0.3 Mn; (**c**) 0.5 Mn; (**d**) 1.0 Mn, and (**e**,**f**) intergranular fracture in a failed specimen.

To further determine the fracture mechanism of the failed specimens, the enlarged fracture surface morphology is presented in Figure 8a–d. As shown in Figure 8a, the fracture surface of the Mn-free alloy is mainly composed of cleavage planes, exhibiting typical brittle fracture characteristics [40]. As the Mn content increased to 0.3 wt.%, the observed tearing edges indicated a transition from fracture to quasi-cleavage fracture (Figure 8b). Furthermore, the fracture morphology was composed of dimples and cleavage planes for the 0.5 Mn alloy, and the fracture behaviors were a combination of ductile and brittle fractures (Figure 8c). Compared to the 0.2 Mn alloy, the fracture surface of the 1.0 Mn alloy was covered with dense dimples, which were deeper and presented larger fluctuations in tearing edges (Figure 8d). In addition, the crack propagation became more tortuous, indicating the greater toughness of the 1.0 Mn alloy.
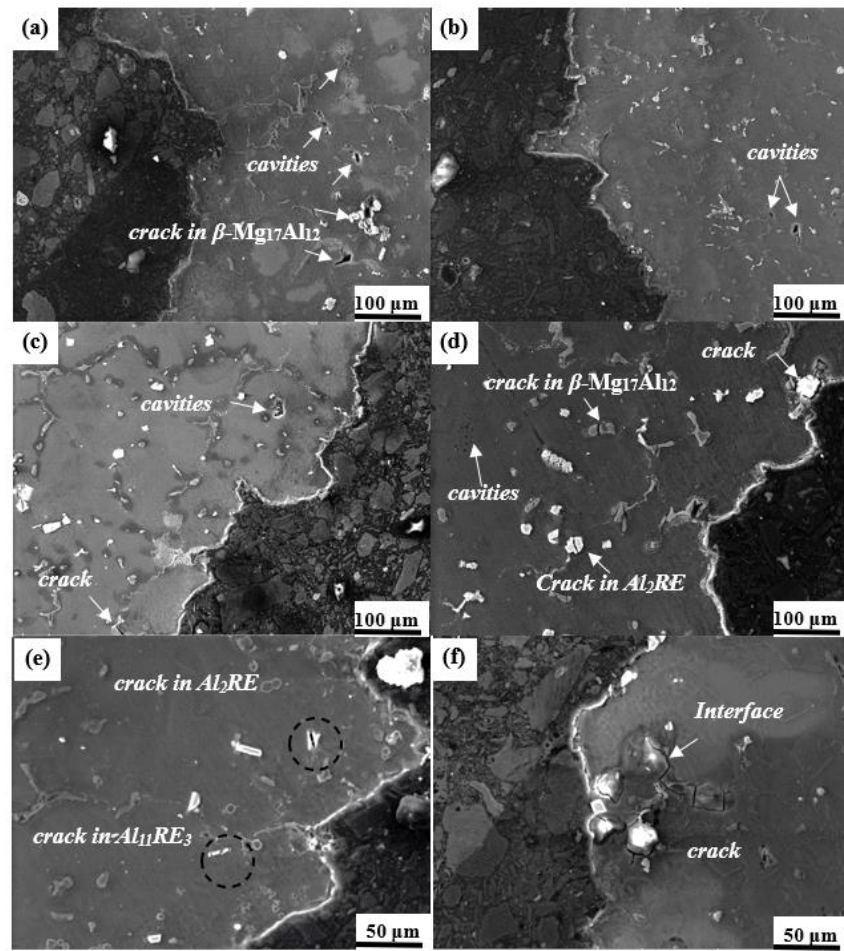
Figure 7. SEM images of cross-section fracture of the tested alloys: (**a**) Mn-free; (**b**) 0.3 Mn; (**c**) 0.5 Mn; (**d**) 1.0 Mn; (**e**) crack in Al_2RE and $Al_{11}RE_3$; and (**f**) the propagation mode of the main crack.
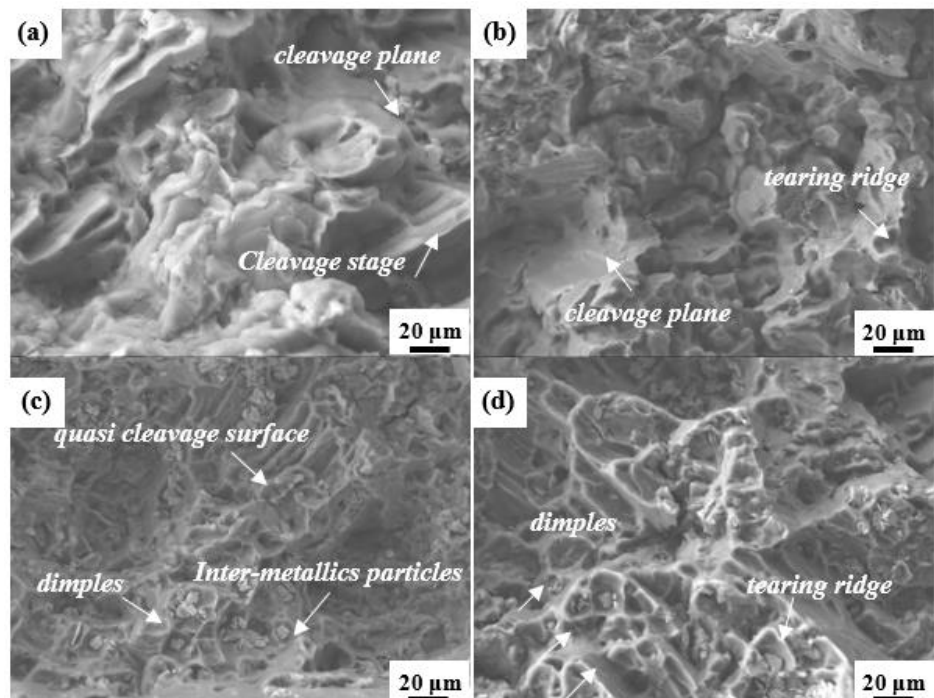

Figure 8. Microscopic fracture morphology of cracks: (**a**) Mn-free; (**b**) 0.3 Mn; (**c**) 0.5 Mn; (**d**) 1.0 Mn.

It is worth noting that intermetallic compound particles were observed in the dimples, and the size of the second-phase particles determines the size of the dimples. According to the energy spectrum of the 1.0 Mn alloy shown in Figure 9a–d, the particles in the dimples were mainly Al-Mn-RE phases, which can effectively hinder dislocation movement and promote the formation of dislocation accumulation, thereby improving the strength of the 1.0 Mn alloy [41,42].
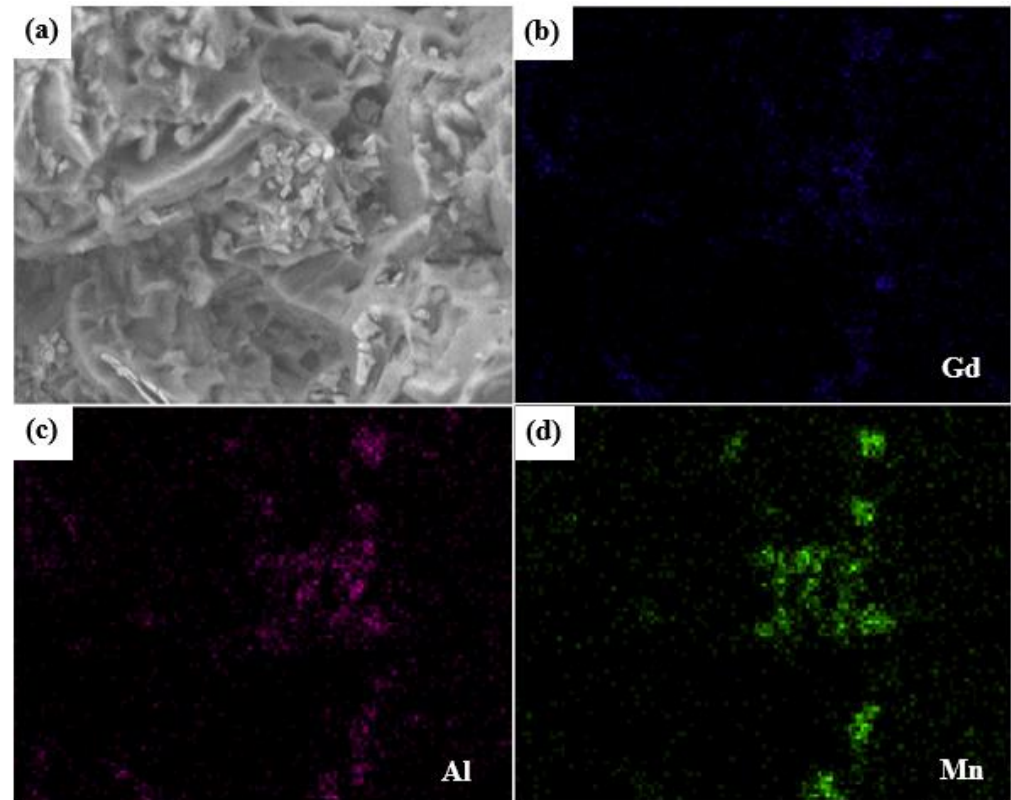

Figure 9. (**a**) Typical SEM backscattered image of the 1.0 Mn alloy with numerous intermetallic compound particles and element mapping of (**b**) Gd, (**c**) Al, and (**d**) Mn.

It can be concluded that the coarse eutectic β-$Mg_{17}Al_{12}$ in the Mn-free alloy is the dominant factor leading to cleavage fracture. The strength of grain boundaries worsened due to β-$Mg_{17}Al_{12}$ during tensile deformation. With the addition of Mn, the coarse β-$Mg_{17}Al_{12}$ was replaced by Al-RE and Al-Mn-RE phases with high elastic moduli, resulting in dispersion strengthening. These dispersed particles effectively hinder dislocation slip during deformation, thereby alleviating stress concentration and coordinating grain deformation of the alloys [43]. This provides a reasonable explanation for the transition from cleavage fracture to ductile fracture.

Figure 10a shows the representative BF-TEM image of the Al-Mn-RE phase; it can be observed that stress concentration caused the initiation of microcracks. According to the selected diffraction pattern in Figure 10b, the intermetallics can be identified as $Al_{10}Mn_2RE$. Moreover, the high-density dislocation near the fracture of the 1.0 Mn alloy is displayed in Figure 10c, and the high density of the edge dislocations can be seen in the crystal plane (Figure 10d) by performing a Fourier transform on dislocation regions, which further confirms that the sustained plastic deformation is related to dislocation slipping.
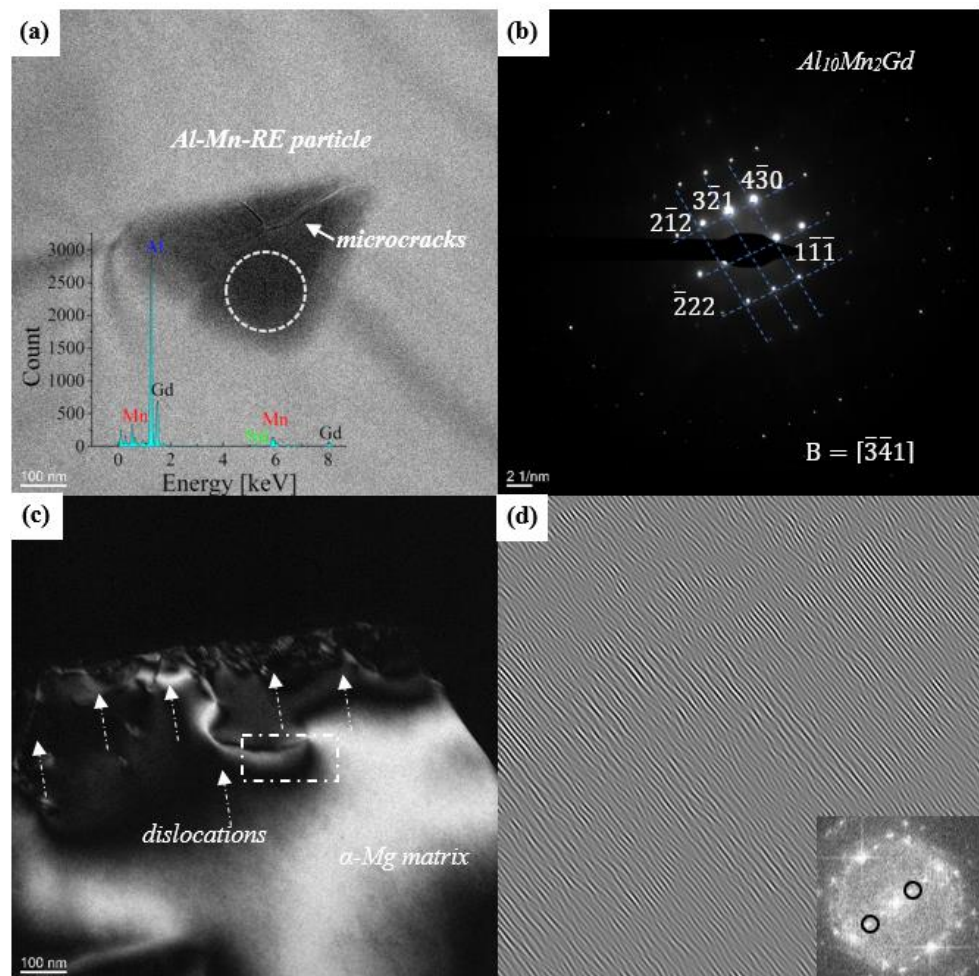
Figure 10. (**a**) BF-TEM micrograph and EDS of the Al-Mn-RE phase; (**b**) corresponding selected diffraction patterns of $Al_{10}Mn_2Gd$; (**c**) the dislocation morphology of the 1.0 Mn alloy with an elongation of 9.8%; and (**d**) the Fast Fourier transform of the dislocation region in the α-Mg matrix.

3.4. Analysis of Activated Twins and Slip Modes

To qualitatively identify the activated twins, in-grain misorientation axes (IGMA) analysis was performed on the tensile deformation of α-matrix grains. This method is based on twin-induced lattice rotation and the determination of its rotation axis [44]. As shown in Figure 11a, a large number of deformation twins were activated during the stretching process based on grain boundary character distribution. It has been reported that high-density twins exert an obvious grain refinement hardening effect in Mg-Al-Zn-Mn alloy [16]. The activated twins were dominated by $\langle 10\bar{1}2 \rangle$ tensile twins and $\langle 10\bar{1}2 \rangle$-$\{10\bar{1}2\}$ secondary twins, while small amounts of $\{10\bar{1}1\}$ compressive twins and $\{10\bar{1}1\}$-$\{10\bar{1}2\}$ double twins were detected in the 0.3 Mn alloy (Figure 11b). Compared to the 0.3 Mn alloy, the color gradient in the EBSD crystal orientation map of the 1.0 Mn alloy reflects a larger internal stress (Figure 11c), indicating that the alloy underwent more severe deformation during stretching. It is worth noting that the proportion of $\langle 10\bar{1}2 \rangle$ tensile twins decreased, while the proportion of $\{10\bar{1}1\}$ compressive twins and secondary twins significantly increased (Figure 11d). The results illustrate that the activation of various twins is greatly affected by the concentration of Mn.
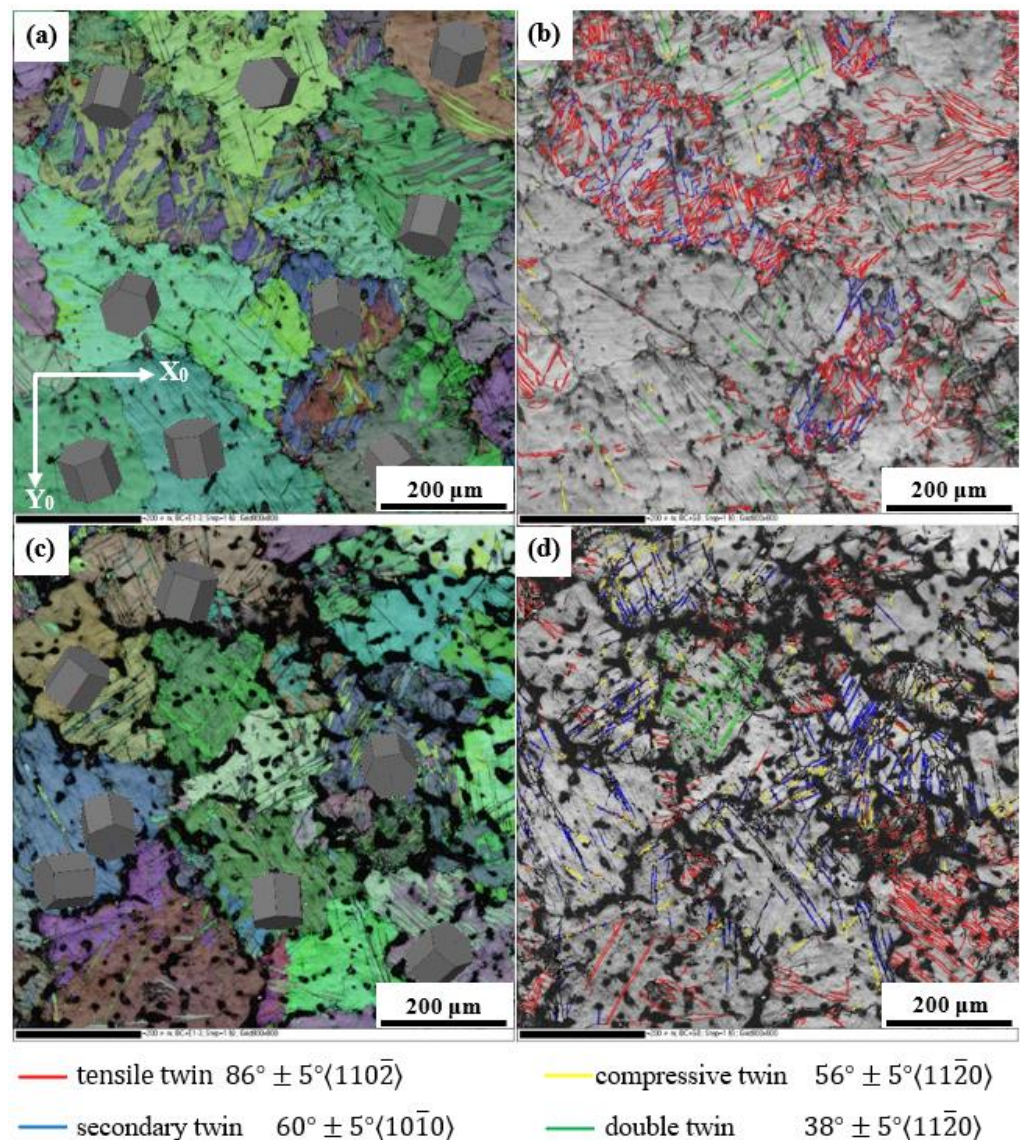
—— tensile twin $86° \pm 5° \langle 110\bar{2} \rangle$	—— compressive twin $56° \pm 5° \langle 11\bar{2}0 \rangle$
—— secondary twin $60° \pm 5° \langle 10\bar{1}0 \rangle$	—— double twin $38° \pm 5° \langle 11\bar{2}0 \rangle$

Figure 11. EBSD with all Euler and distribution of activated twins of tensile deformation structure: (**a**,**b**) 0.3 Mn alloy, (**c**,**d**) 1.0 Mn alloy.

To quantitatively analyze the various twins shown in Figure 11, the statistical results are shown in Table 5. The total proportions of twins in the 0.3 Mn alloy and 1.0 Mn alloy were 23.85% and 23.4%, respectively. It has been confirmed that the $\{10\bar{1}2\}\langle\bar{1}011\rangle$ tensile twins are conducive to the plastic deformation of Mg alloys at room temperature [21,45]. In addition, the $\{10\bar{1}2\}$ twins are beneficial for activating the pyramidal II *<a+c>* slip and coordinating the deformation along the c-axis of the grain [22,46]. Furthermore, the interaction between lattice dislocation and the twin boundary plays a crucial role in the plastic deformation of Mg alloys [47]. The experimental results indicate that both the tensile and compressive twins were activated simultaneously, and the more uniform the distribution, the more favorable the plastic deformation of the alloys. Therefore, appropriately increasing the proportion of $\{10\bar{1}1\}$ twins and $60° \pm 5°\langle10\bar{1}0\rangle$ secondary twins was beneficial to improving the tensile strength. This may be related to the grain refinement of the 1.0 Mn alloy, which leads to more uniform grain deformation under stress and contributes to suppressing crack initiation.

Table 5. Volume fraction of twin variants in tensile fracture specimens.

Activated Twins	Twinning Area Fractions	
	0.3 Mn Alloy (Strain 5.1%)	1.0 Mn Alloy (Strain 9.8%)
$\{10\bar{1}2\}$ tensile twins	20	10.8
$\{10\bar{1}1\}$–$\{10\bar{1}2\}$ double twins	1.5	5.5
$\{10\bar{1}1\}$ compressive twins	0.8	3.9
$\{10\bar{1}2\}$–$\{10\bar{1}2\}$ secondary twins	1.55.	3.2

To further elucidate the deformation mechanism of a 1.0 Mn alloy with excellent plastic deformation ability, the IGMA method was implemented to identify the activated slip modes. The dominant slip system can be inferred in deformed grains by matching the Taylor axis (Table 6) [23,27]. As shown in Figure 12a,b, the results indicate that basal *<a>* and pyramidal *<a>* slip dominated in the 0.3 Mn alloy, while the proportion of prismatic *<a>* slip was very low, resulting in a weak distribution of intensities along the <0001> axis. As the Mn content increased to 1.0 wt.%, the prismatic *<a>* slip increased significantly. Accordingly, the basal *<a>* slip, accompanied by the prismatic *<a>* slip, which leads to a cross slip, is crucial for improving the plasticity of the alloy [48]. The addition of a solid solution of Mn atoms into the Mg matrix may lead to a change in the lattice parameter *c/a* ratio, thereby affecting the critical shear stress of the slip modes, which needs to be elaborated upon. The excellent elongation of the 1.0 Mn alloy is attributed to the significant activation of prismatic *<a>* slip and the increase in the proportion of compressive twins.

Table 6. Activated slip modes in Mg and the corresponding Taylor axes.

Activated Slip	Deformation Mode	Variants	Taylor Axis
Basal *<a>*	$\{0001\}\langle11\bar{2}0\rangle$	3	$\langle01\bar{1}0\rangle$
Prismatic *<a>*	$\{10\bar{1}0\}\langle11\bar{2}0\rangle$	3	$\langle0001\rangle$
Pyramidal *<a>*	$\{10\bar{1}1\}\langle11\bar{2}0\rangle$	6	$\langle11\bar{2}0\rangle$
Pyramidal *<a+c>*	$\{11\bar{2}2\}\langle11\bar{2}3\rangle$	6	$\langle1\bar{1}00\rangle$
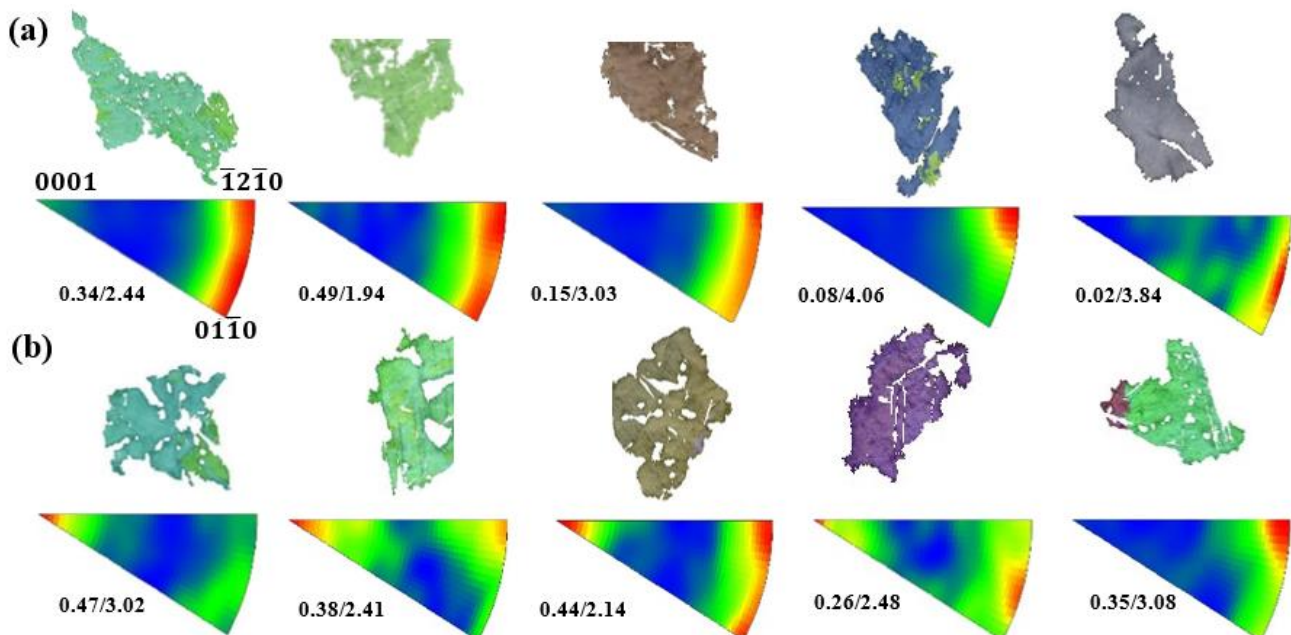
Figure 12. Deformed grains and corresponding IGMA distributions: (**a**) 0.3 Mn alloy; (**b**) 1.0 Mn alloy. The min/max intensities of the IGMA distribution are illustrated in the corresponding figure.

4. Conclusions

In this work, the influence of Mn modification on the mechanical properties of Mg-Al-RE alloys was discussed. The addition of Mn promotes the precipitation of various intermetallic compounds while promoting the activation of prismatic <*a*> slip, which can significantly improve the plastic deformation ability of the alloy. It is of great significance for improving the ductility of heat-resistant Mg-Al-RE alloys.

(1) The addition of Mn transforms continuous island-shaped eutectic β-$Mg_{17}Al_{12}$ into dispersed granular divorced eutectic particles and promotes the precipitation of $Al_{10}Mn_2$ (Nd,Gd) and Al_8 (Nd,Gd)Mn_4.
(2) The $Al_{10}Mn_2$ (Nd,Gd) particles can effectively hinder the slip of intragranular dislocations and alleviate stress concentration at grain boundaries. The dimples in the tensile fracture confirm the transition of the fracture mode from cleavage fracture to ductile fracture.
(3) The combination of activated prismatic <*a*> slip and deformation twinning enhances the plastic deformation ability of the Mg-Al-RE alloy.

Author Contributions: Methodology, J.Y. and W.W.; software, M.Z.; data curation, J.L.; writing—original draft preparation, J.Y. and S.Q.; review and editing, W.W. and M.Z. All authors have read and agreed to the published version of the manuscript.

Institutional Review Board Statement: Not applicable.

Informed Consent Statement: Not applicable.

Data Availability Statement: The data presented in this study are available on request from the corresponding author.

Conflicts of Interest: The authors declare no conflict of interest.

References

1. Song, J.; She, J.; Chen, D.; Pan, F. Latest research advances on magnesium and magnesium alloys worldwide. *J. Magnes. Alloys* **2020**, *8*, 1–41. [CrossRef]
2. Zeng, Z.; Stanford, N.; Davies, C.H.J.; Nie, J.F.; Birbilis, N. Magnesium extrusion alloys: A review of developments and prospects. *Int. Mater. Rev.* **2019**, *64*, 27–62. [CrossRef]
3. Ma, G.; Xiao, H.; Ye, J.; He, Y. Research status and development of magnesium matrix composites. *Mater. Sci. Technol.* **2020**, *36*, 645–653. [CrossRef]
4. Mo, N.; Tan, Q.; Bermingham, M.; Huang, Y.; Dieringa, H.; Hort, N.; Zhang, M.X. Current development of creep-resistant magnesium cast alloys: A review. *Mater. Des.* **2018**, *155*, 422–442. [CrossRef]
5. Cai, H.; Guo, F.; Su, J.; Liu, L. Thermodynamic analysis of Al-RE phase formation in AZ91-RE (Ce, Y, Gd) magnesium alloy. *Phys. Status Solidi B Basic Res.* **2020**, *257*, 1900453. [CrossRef]
6. Ashrafizadeh, S.M.; Mahmudi, R. Effects of Gd, Y, and La rare-earth elements on the microstructural stability and elevated-temperature mechanical properties of AZ81 magnesium alloy. *Metall. Mater. Trans. A* **2019**, *50*, 5957–5968. [CrossRef]
7. Lv, S.; Li, Y.; Meng, F.; Duan, Q.; Yang, Q.; Liu, X.; Meng, J. Thermodynamic stability of $Al_{11}RE_3$ intermetallic compounds from first-principles calculations. *Comput. Mater. Sci.* **2017**, *131*, 28–34. [CrossRef]
8. Zhu, S.M.; Gibson, M.A.; Nie, J.F.; Easton, M.A.; Abbott, T.B. Microstructural analysis of the creep resistance of die-cast Mg-4Al-2RE alloy. *Scr. Mater.* **2008**, *58*, 477–480. [CrossRef]
9. Yang, Q.; Guan, K.; Bu, F.; Zhang, Y.; Qiu, X.; Zheng, T.; Liu, X.; Meng, J. Microstructures and tensile properties of a high-strength die-cast Mg-4Al-2RE-2Ca-0.3Mn alloy. *Mater. Charact.* **2016**, *113*, 180–188. [CrossRef]
10. Qin, P.F.; Yang, Q.; Guan, K.; Meng, F.Z. Microstructures and mechanical properties of a high pressure die-cast Mg-4Al-4Gd-0.3Mn alloy. *Mater. Sci. Eng. A* **2019**, *764*, 138254. [CrossRef]
11. Qin, G.W.; Ren, Y.; Huang, W.; Li, S.; Pei, W. Grain refining mechanism of Al-containing Mg alloys with the addition of Mn-Al alloys. *J. Alloys Compd.* **2010**, *507*, 410–413. [CrossRef]
12. Braszczyńska-Malik, K.N.; Grzybowska, A. Microstructure of Mg-5Al-0.4Mn-*x*RE (*x* = 3 and 5 Wt.%) alloys in as-cast conditions and after annealing. *J. Alloys Compd.* **2016**, *663*, 172–179. [CrossRef]

13. Yang, Q.; Guan, K.; Li, B.; Lv, S.; Meng, F.; Sun, W.; Zhang, Y.; Liu, X.; Meng, J. Microstructural characterizations on Mn-containing intermetallic phases in a high-pressure die-casting Mg-4Al-4RE-0.3Mn Alloy. *Mater. Charact.* **2017**, *132*, 381–387. [CrossRef]

14. Su, M.; Zhang, J.; Feng, Y.; Bai, Y.; Wang, W.; Zhang, Z.; Jiang, F. Al-Nd intermetallic phase stability and its effects on mechanical properties and corrosion resistance of HPDC Mg-4Al-4Nd-0.2Mn alloy. *J. Alloys Compd.* **2017**, *691*, 634–643. [CrossRef]

15. Li, Z.T.; Qiao, X.G.; Xu, C.; Liu, X.Q.; Kamado, S.; Zheng, M.Y. Enhanced strength by precipitate modification in wrought Mg-Al-Ca alloy with trace Mn addition. *J. Alloys Compd.* **2020**, *836*, 154689. [CrossRef]

16. Li, J.; Xie, D.; Yu, H.; Liu, R.; Shen, Y.; Zhang, X.; Yang, C.; Ma, L.; Pan, H.; Qin, G. Microstructure and mechanical property of multi-pass low-strain rolled Mg-Al-Zn-Mn alloy sheet. *J. Alloys Compd.* **2020**, *835*, 155228. [CrossRef]

17. Zhu, S.M.; Abbott, T.B.; Gibson, M.A.; Nie, J.F.; Easton, M.A. The influence of minor Mn additions on creep resistance of die-cast Mg-Al-RE alloys. *Mater. Sci. Eng. A* **2017**, *682*, 535–541. [CrossRef]

18. Yang, Q.; Yan, Z.; Lv, S.; Guan, K.; Qiu, X. Abnormal creep stress exponents in a high-pressure die casting Mg-Al-RE alloy. *Mater. Sci. Eng. A* **2022**, *831*, 142203. [CrossRef]

19. Liao, Q.; Chen, X.; Lan, Q.; Ning, F.; Le, Q. The effect of double extrusion on the microstructure and mechanical properties of AZ80RE alloy. *Mater. Res. Express* **2018**, *5*, 126510. [CrossRef]

20. Niknejad, S.; Esmaeili, S.; Zhou, N.Y. The Role of Double twinning on transgranular fracture in magnesium AZ61 in a localized stress field. *Acta Mater.* **2016**, *102*, 1–16. [CrossRef]

21. Deng, J.-f.; Tian, J.; Chang, Y.; Zhou, Y.; Liang, W.; Ma, J. The role of $\{10\bar{1}2\}$ tensile twinning in plastic deformation and fracture prevention of magnesium alloys. *Mater. Sci. Eng. A* **2022**, *853*, 143678. [CrossRef]

22. Tian, J.; Deng, J.-f.; Chang, Y.; Zhou, Y.; Liang, W.; Ma, J. Selection behavior of $\{10\bar{1}2\}$ tensile twin variants and its contribution during plastic processing of magnesium alloy. *J. Alloys Compd.* **2022**, *918*, 165517. [CrossRef]

23. Chun, Y.B.; Davies, C.H.J. Investigation of prism <a> slip in warm-rolled AZ31 alloy. *Metall. Mater. Trans. A* **2011**, *42*, 4113–4125. [CrossRef]

24. Mulay, R.P.; Agnew, S.R. Hard slip mechanisms in B_2CoTi. *Acta Mater.* **2012**, *60*, 1784–1794. [CrossRef]

25. Chun, Y.B.; Battaini, M.; Davies, C.H.J.; Hwang, S.K. Distribution characteristics of in-grain misorientation axes in cold-rolled commercially pure titanium and their correlation with active slip modes. *Metall. Mater. Trans. A* **2010**, *41*, 3473–3487. [CrossRef]

26. Yang, B.; Shi, C.; Ye, X.; Teng, J.; Lai, R.; Cui, Y. Underlying slip/twinning activities of Mg-*x*Gd alloys investigated by modified lattice rotation analysis. *J. Magnes. Alloys* **2023**, *11*, 998–1015. [CrossRef]

27. Zhang, M.; Luan, B.; Chu, L.; Gao, B.; Wang, L.; Yuan, G. Deformation kinking in *β*-treated zirconium impacted by split hopkinson pressure Bar. *Scr. Mater.* **2020**, *187*, 379–383. [CrossRef]

28. Lv, S.; Lü, X.; Meng, F.; Yang, Q.; Qiu, X.; Qin, P.; Duan, Q.; Meng, J. Microstructures and mechanical properties in a Gd-modified high-pressure die casting Mg-4Al-3La-0.3Mn alloy. *Mater. Sci. Eng. A* **2020**, *773*, 138725. [CrossRef]

29. Liu, H.; Zuo, J.; Nakata, T.; Xu, C.; Wang, G.; Shi, H.; Tang, G.; Wang, X.; Kamado, S.; Geng, L. Effects of La addition on the microstructure, thermal conductivity and mechanical properties of Mg-3Al-0.3Mn alloys. *Materials* **2022**, *15*, 1078. [CrossRef]

30. Singh, L.K.; Bhadauria, A.; Srinivasan, A. Effects of gadolinium addition on the microstructure and mechanical properties of Mg-9Al alloy. *Int. J. Miner. Metall. Mater.* **2017**, *24*, 901–908. [CrossRef]

31. Tekumalla, S.; Seetharaman, S.; Almajid, A.; Gupta, M. Mechanical properties of Magnesium-Rare Earth Alloy Systems: A Review. *Metals* **2015**, *5*, 1–39. [CrossRef]

32. Deming, G.; Yuhui, Z.; Qin, H.; Qiqie, Z. Study on mechanical properties of Mg-Al-Zn-Mn alloys cast by two different methods. *Mater. Sci. Eng. A* **2009**, *507*, 1–5. [CrossRef]

33. Jiang, N.; Meng, L.G.; Zhang, X.G.; Chen, L.; Fang, C.F.; Hao, H. Microstructure and mechanical properties of Gd-modified AZ80 magnesium alloys. *Rare Met.* **2022**, *41*, 4194–4200. [CrossRef]

34. Li, Z.; Gao, T.; Xu, Q.; Yang, H.; Han, M.; Liu, X. Microstructure and mechanical properties of an AlN/Mg-Al composite synthesized by Al-AlN master alloy. *Int. J. Met.* **2019**, *13*, 384–391. [CrossRef]

35. Zhu, S.; Easton, M.A.; Abbott, T.B.; Nie, J.F.; Dargusch, M.S.; Hort, N.; Gibson, M.A. Evaluation of magnesium die-casting alloys for elevated temperature applications: Microstructure, tensile properties, and creep resistance. *Metall. Mater. Trans. A Phys. Metall. Mater. Sci.* **2015**, *46*, 3543–3554. [CrossRef]

36. Yu, H.; Xin, Y.; Wang, M.; Liu, Q. Hall-Petch pelationship in Mg alloys: A review. *J. Mater. Sci. Technol.* **2018**, *34*, 248–256. [CrossRef]

37. Hu, F.; Zhao, S.; Gu, G.; Ma, Z.; Wei, G.; Yang, Y.; Peng, X.; Xie, W. Strong and ductile Mg-0.4Al alloy with minor Mn addition achieved by conventional extrusion. *Mater. Sci. Eng. A* **2020**, *795*, 139926. [CrossRef]

38. Li, Y.X.; Zhou, Z.; Wang, L.; Cheng, H.W.; Cheng, X.W. Research on dynamic fracture behavior of Ti6321 titanium alloy. *Rare Met. Mater. Eng.* **2023**, *52*, 953–958.

39. Cui, X.; Yu, Z.; Liu, F.; Du, Z.; Bai, P. Influence of secondary phases on crack initiation and propagation during fracture process of as-cast Mg-Al-Zn-Nd alloy. *Mater. Sci. Eng. A* **2019**, *759*, 708–714. [CrossRef]

40. Xie, H.; Wu, G.; Zhang, X.; Liu, W.; Ding, W. Materials characterization the role of Gd on the microstructural evolution and mechanical properties of Mg-3Nd-0.2Zn-0.5Zr alloy. *Mater. Charact.* **2021**, *175*, 111076. [CrossRef]

41. Meng, F.; Lv, S.; Yang, Q.; Qin, P.; Zhang, J.; Guan, K.; Huang, Y.; Hort, N.; Li, B.; Liu, X.; et al. Developing a die casting magnesium alloy with excellent mechanical performance by controlling intermetallic phase. *J. Alloys Compd.* **2019**, *795*, 436–445. [CrossRef]

42. Wang, J.; Dong, H.; Wang, L.; Wu, Y.; Wang, L. Effect of hot rolling on the microstructure and mechanical properties of Mg-5Al-0.3Mn-2Nd Alloy. *J. Alloys Compd.* **2010**, *507*, 178–183. [CrossRef]
43. Ercetin, A.; Özgün, Ö.; Aslantaş, K.; Der, O.; Yalçın, B.; Şimşir, E.; Aamir, M. Microstructural and mechanical behavior investigations of Nb-reinforced Mg-Sn-Al-Zn-Mn matrix magnesium composites. *Metals* **2023**, *13*, 1097. [CrossRef]
44. Guan, D.; Rainforth, W.M.; Ma, L.; Wynne, B.; Gao, J. Twin recrystallization mechanisms and Exceptional Contribution to texture evolution during annealing in a magnesium alloy. *Acta Mater.* **2017**, *126*, 132–144. [CrossRef]
45. Guo, C.; Xin, R.; Zheng, X.; Xiao, Y.; Ding, C.; Liu, Q. Influence of observation plane on twin variant identification in magnesium via trace and misorientation analysis. *Mater. Sci. Eng. A* **2014**, *618*, 558–562. [CrossRef]
46. Guan, D.; Wynne, B.; Gao, J.; Huang, Y.; Rainforth, W.M. Basal slip mediated tension twin variant selection in magnesium WE43 alloy. *Acta Mater.* **2019**, *170*, 1–14. [CrossRef]
47. Zhang, J.; Xi, G.; Wan, X.; Fang, C. The dislocation-twin interaction and evolution of twin boundary in AZ31 Mg alloy. *Acta Mater.* **2017**, *133*, 208–216. [CrossRef]
48. Jiang, S.; Jia, Y.; Wang, X.; Jiang, J. Materials characterization precise measurement of strain accommodation in a Mg-Gd-Y-Zn alloy using cross-correlation-based high resolution EBSD. *Mater. Charact.* **2020**, *165*, 110384. [CrossRef]